applied sciences

MDPI

Article

Experimental Investigation of the Creep Behaviour of Coal by Monitoring Changes of Acoustic Properties

Sen Yang [1,2], Nong Zhang [1,*], Xiaowei Feng [1] and Jiaguang Kan [1]

1 Key Laboratory of Deep Coal Resource Mining, Ministry of Education of China, School of Mines, China University of Mining and Technology, Xuzhou 221116, China; yangsen2009@outlook.com (S.Y.); fxw_mining@foxmail.com (X.F.); jgkan@126.com (J.K.)

2 Department of Energy and Mineral Engineering, G3 Center and Energy Institute, The Pennsylvania State University, University Park, PA 16802, USA

* Correspondence: zhangnong@cumt.edu.cn; Tel.: +86-516-8359-0502

Received: 5 March 2018; Accepted: 18 April 2018; Published: 19 April 2018

Abstract: Time-dependent deformation of coal is a major concern for deep coal mining. When experiencing high stress conditions, the enhanced time-dependent deformation of coal will become a very possible factor to trigger the violent failure of underground openings. For this study, the inner structural variation of an extremely inhomogeneous coal subjected to incremental creep stress has been experimentally investigated by monitoring both the macroscopic deformation and acoustic property. Results show the following: (1) The pronounced inhomogeneity of coal induces considerable irregularities in creep strain data collected during the increase of stress level. These flawed data highlight the shortcomings of conventional strain-time relationship experiments for deciphering the mechanisms that control creep; (2) The mechanical response of samples under creep compression is the result of competition between compaction and cracking. Cracking deteriorates the structure and increases the ultrasonic attenuation, whilst the compaction causes the densification along the axial axis and reduces attenuation; (3) Long-term creep involves multiple structural deformations that alter the internal structure of the coal. This results in fluctuations of the ultrasonic velocities and their dynamic moduli; (4) During uploading phase of short term creep, vertical cracks develop and transform the sample into a structure consisting of separated columns. Further deterioration of the coal increases the possibility of tensile and shear failure of individual columns, which can trigger the violent collapse of an already fragile structure.

Keywords: coal creep; acoustic attenuation; wave velocity; long-term ground stability

1. Introduction

In 2016, the coal-fired power generation accounted for 37% of the world's electricity generation capacity, and the share is predicted to be above 30% over the next decade [1]. Therefore, coal production is playing a very important role in the global economy. However, long-term ground stability is becoming a major concern to the coal mining industry [2]. Underground coal mines commonly operate at a depth of hundreds of metres, and some very deep mines even reach and exceed one thousand metres [3]. Deep mining is accompanied by high overburden stresses, complex geologic conditions, and, in some cases, tectonic stresses [4]. In addition, typical coal-measure sedimentary rocks are relatively weak, especially the coal. When experiencing high stress conditions, the time-dependent deformation of coal over time is significant and can become a very important factor in triggering the violent failure of underground openings.

Creep is the name applied for the time-dependent deformation of solids resulting from constant stress [5]. The discovery of the creep of rock and rock-like materials can be tracked back to 1907; Hatt [6]

observed a slow deformation of concrete under a constant environmental condition. Since then, many studies have been devoted to improving the understanding of concrete creep. Successes have been achieved both in the physical mechanism and the mathematical model. Physical mechanisms proposed for concrete creep can be summarized as plastic flow [7,8], nonlinear cracking and reformation [9–11], and solidification theory [12,13]. The mathematical models are established mainly for two purposes: facilitation of structural analysis and close agreement with experimental data. Based on the effective modulus method [14,15], the rate-of-creep model [16], rate-of-flow model [17], and Arutyunian-Maslov model [18] were proposed to simplify the structural analysis. The B3 model [19] and Double power law [20] were formulated with a view to improve the data fitting and predication. In term of progresses in rock creep, the pioneering work was done by Griggs [21] who first developed two types of apparatus to investigate the creep behaviour of shale and limestone. Since then, extensive investigations have been conducted on the time-dependent behaviour of many different rocks by using experimental, theoretical, and in situ approaches [22–33]. When being expressed as a function of time, it develops in three stages: primary (transient) creep, secondary (steady) creep, and tertiary (accelerating) creep (as illustrated in Figure 1). Prior to the primary stage of creep, instantaneous elastic strain is generated as the first response of the rock to the applied stress. Several researchers suggested considering the instantaneous strain as a part of creep process [34,35]. As time passes, the strain increases without any change of the applied stress. At the primary stage, the strain rate gradually decreases, and the creep strain is governed by the elastic deformation mechanism [36]. During the secondary stage, the strain rate stabilises at a nearly constant value, the behaviour of which is determined by the visco-plastic properties of rock [34,37]. If the secondary stage is allowed to continue, then the strain rate begins to increase (tertiary stage). The tertiary stage accounts for only a small portion of rock lifetime. However, it is associated with the structural failure caused by the process of micro-fracturing, and therefore it is crucial in predicating service life of rock and rock mass.

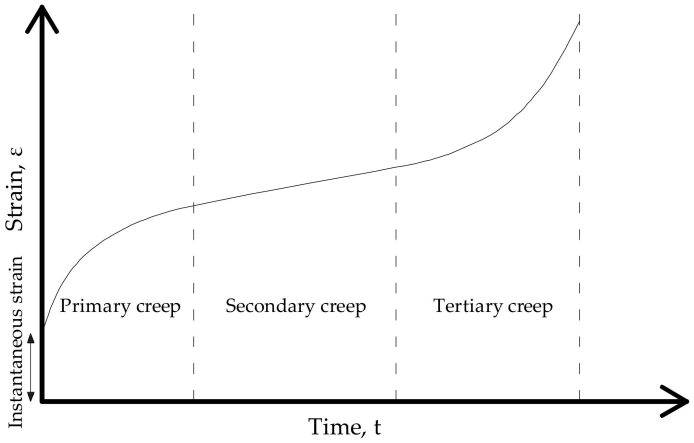

Figure 1. Schematic graph illustrating the three classical stages of creep for rock.

Compared to the fruitful investigations of creep in rock salt, shale, and sandstone, very few results on creep in coal have been reported. Pomeroy [38] investigated the time-dependent behaviour of stress on bituminous coal and anthracite by performing compression and bending tests. The results showed that an extremely slow strain rate may induce the non-explosive breakage of bituminous coal but cannot prevent the explosive breakage of anthracite. Kasier and Morgenstern [39] estimated the time-dependent deformation of laboratory-scale simulated tunnels excavated in a block of subbituminous coal. Kang et al. [36] combined the fractional elements in a non-linear mathematical model in order to describe coal creep. This model successfully reproduced tertiary creep. By introducing a damage factor into Burgers creep model, Yang et al. [40] developed a non-linear model to describe creep in coal, and this model agreed very well with the results of triaxial creep compression

tests. Most of the previous studies on coal creep mainly paid attention to the macroscopic deformation of the coal and phenomenological models but made negligible effort to the inner microstructural variations in the coal. Coal's macroscopic deformation is a consequence of the evolution of inner microstructural readjustments such as pore closure, crack growth, and grain displacement. However, owing to the invisibility of the inner microstructures and the long duration of creep tests, it is nearly impossible to deploy conventional methods such as optical microscope and scanning electron microscope (SEM) to track these changes.

In this work, an indirect measurement, acoustic detection, is used to monitor the inner structural changes in an extremely inhomogeneous coal subjected to incremental creep stress. By interpreting the velocity, attenuation, and dynamic modulus of ultrasonic waves, the deformational mechanisms underlying the macroscopic deformation are examined.

2. Experimental Procedures

Cylindrical samples used in these experiments were drilled from the same block of anthracite, a block collected from an open-pit mine located in Hazle, Pennsylvania, USA. The drilling direction was kept perpendicular to the beddings. The desired diameter to height ratio for the cores was 1:2. However, several trial drillings demonstrated that the extremely cataclastic texture of the anthracite block did not make this possible. By reducing the ratio to 1:1.45, 11 cores were obtained with nominal dimensions of $\Phi 45 \times 65$ mm. Subsequently, the ends of the sample were ground and polished according to ISRM standards [41]. Typical samples prepared for the test are shown in Figure 2. In order to eliminate the influence of water, the samples were oven-dried until their weight remained constant.

Figure 2. Typical samples prepared for the test.

The experiment was conducted in a basement with a constant temperature of 16 ± 2 °C. A series of creep tests under uniaxial compression were performed on a servo-controlled hydraulic testing machine (shown in Figure 3). The machine had a load frame of stiffness 6000 kN/mm and a compression load capacity of 1000 kN with a resolution of 0.5%. Its stroke was ±50 mm with a resolution of 1 µm. The tests were performed using 11 pre-set stress levels ranging from 8 MPa to 18 MPa, each level being increased by 1 MPa. However, because of the inevitable variations in the diameters of the cores produced during drilling, the actual stress values applied in the tests (shown in Table 1) differed slightly. For the tests, creep stress was applied by increasing the loading force to the prescribed level at a constant rate 100 N/s. The pre-set duration of each stress level is 6 h. Commercially available piezoelectric transducers with a 200 kHz main frequency were used for both transmitting and receiving the ultrasonic signals. As illustrated in Figure 3, one piezoelectric transducer, the transmitter, was placed between the upper face of specimen and the fixed end of the hydraulic platen, and the receiving transducer was located between the bottom face of the specimen and the lower (loading) end of the platen. The ultrasonic measurement was acquired and recorded using a digital system consisting of a pulse generator, time measuring circuit, receiver amplifier, and time-display unit. The sampling interval of ultrasonic signal was 3 min.

Table 1. Applied stresses and secondary strain rates for the creep compression tests.

Creep Stress (MPa)	Axial Strain Rate (per hour)	Radial Strain Rate (per hour)	Volumetric Strain Rate (per hour)
8.03	1.59×10^{-4}	-1.08×10^{-5}	1.38×10^{-4}
8.98	2.53×10^{-4}	-1.26×10^{-4}	1.04×10^{-6}
10.00	3.29×10^{-5}	-6.35×10^{-5}	-9.41×10^{-5}
11.02	1.92×10^{-3}	-4.91×10^{-3}	-7.89×10^{-3}
11.98	1.06×10^{-4}	-2.27×10^{-5}	6.07×10^{-5}
13.00	2.11×10^{-4}	-2.32×10^{-5}	1.65×10^{-4}
14.02	2.49×10^{-4}	-4.47×10^{-5}	1.60×10^{-4}
14.97	1.36×10^{-4}	-9.59×10^{-5}	-3.02×10^{-6}
15.99	5.63×10^{-3}	-2.54×10^{-2}	-4.53×10^{-2}
17.01	1.85×10^{-4}	-4.01×10^{-5}	1.04×10^{-4}
17.97	4.66×10^{-3}	-5.23×10^{-2}	-1.00×10^{-1}

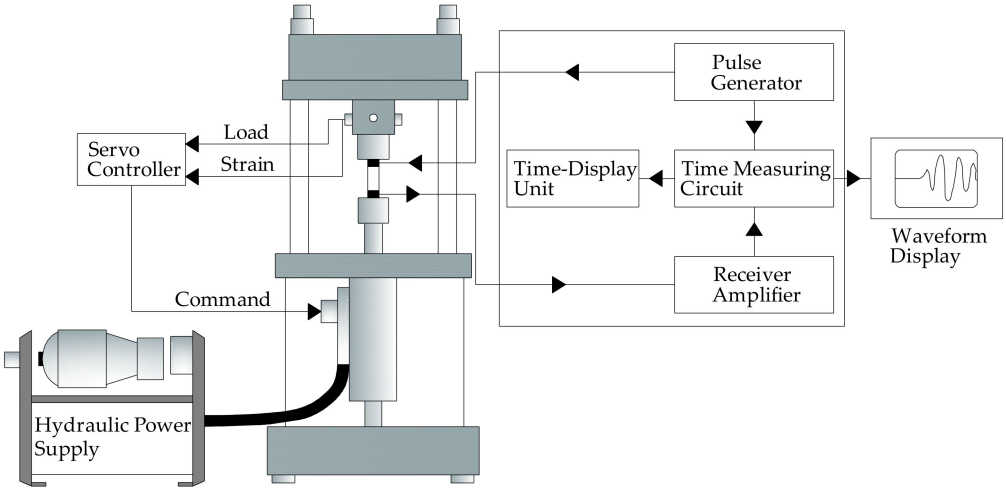

Figure 3. Schematic diagram for the equipment configuration.

3. Results and Discussion

3.1. Creep Behaviour of Coal

The creep strain and increasing stress did not follow the monotonous incremental path expected. On the contrary, two rapid collapses at relatively low stress levels, 15.99 MPa and 11.02 MPa, occurred. Table 1 lists the calculated strain rates for the secondary stages of the creep tests. The results scatter considerably and no convincing correlation can be established between creep strain and stress level. Although the samples were drilled from the same block of coal, their creep behaviour varied significantly, indicating pronounced inhomogeneity between samples.

Because the attempt to demonstrate a relationship between creep and stress failed, the samples were classified according to creep behaviour. The creep curves are divided into three types—Types 1, 2, and 3.

On Type 1 curves, (Figure 4a), the axial strain (ε_a) clearly exhibits primary and secondary creep but the radial strain (ε_r) creeps at a slow but relatively steady rate for the entire duration of the experiment. Another important feature of this Type is that the volumetric strain (ε_v) is dominated by axial strain, reflecting the compression. This relationship can also be observed in the highly similar trends of volumetric strain rate (r_v) and axial strain rate (r_a) shown in Figure 5a or Figure 5c. Both rates increase from the initial point to a peak value, then reverse direction and gradually decline before reaching a stable stage (the stable stage corresponds to secondary creep). Figure 5b presents the change in radial strain rate (r_r) for Type 1 creep. It can be seen that r_r steeply decelerates (the increasingly

negative strain rates) from the initial dilatancy to a relatively stable stage. Compared to volumetric and axial strain rates, the radial strain rate is fairly low. The results from these tests have a moderate amount of scatter. It causes difficulties in identifying the transition point from the primary creep to the secondary creep. In order to facilitate further analysis, equations were fit to the r_a, r_v, and r_r data, and these are presented below as Equations (1)–(3).

$$r_a = \left(-3.3t^6 + 111.9t^5 - 1488.7t^4 + 9732.9t^3 - 31344t^2 + 39750.2t + 2738\right) \times 10^{-4}\left(R^2 = 0.94\right), \quad (1)$$

$$r_v = \left(-3.7t^6 + 124.3t^5 - 1654.4t^4 + 10817t^3 - 34908t^2 + 45097.1t + 241.2\right) \times 10^{-4}\left(R^2 = 0.94\right), \quad (2)$$

$$r_r = \left(-0.5t^6 + 13.9t^5 - 154.2t^4 + 858.6t^3 - 2460.3t^2 + 3302.5t + 1659.1\right) \times 10^{-4}\left(R^2 = 0.55\right), \quad (3)$$

where t denotes time. As described above, the axial deformation is the dominate mechanism of this type of creep process. Through examining the derivation of Equation (1), the primary creep and the secondary creep are identified and shown in Figure 4a. It can be observed that the primary creep takes up a large portion of the test duration and then transforms into the secondary creep. Another long duration of the secondary creep can also be expected. Type 1 creep occurs at pressures of 8.03, 8.98, 11.98, 13.00, 14.0,2 and 14.97 MPa.

Type 2 creep, dilatancy caused by loading, dominates initial deformation (Figure 4b). Approximately 20 min after the load is first imposed, the increasing axial strain cannot be balanced by radial strain, thus the volumetric strain reverses direction to follow the trend of the axial strain. This marks the beginning of compaction. Despite the drastic dilatancy developing in the uploading phase, secondary creep can still be observed on the axial strain curve, which suggests that microcracks developed parallel to the loading direction (in this case, it is the axis of the sample) have only a slight influence on the axial strain. Overall, the strain rates exhibit similar variations with Type 1 except for the initial high value of the radial strain rate (Figure 6). The fitting formulas for Type 2 creep are

$$r_a = \left(-5.8t^6 + 178t^5 - 2169.1t^4 + 13095t^3 - 39481t^2 + 48343.7t + 516.7\right) \times 10^{-4}\left(R^2 = 0.95\right), \quad (4)$$

$$r_v = \left(-11.2t^6 + 339.7t^5 - 4073.8t^4 + 24228t^3 - 72927t^2 + 96083.3t - 24862\right) \times 10^{-4}\left(R^2 = 0.90\right), \quad (5)$$

$$r_r = \left(-15.1t^6 + 348.4t^5 - 3158.5t^4 + 14247t^3 - 33269t^2 + 37509t - 16195.5\right) \times 10^{-4}\left(R^2 = 0.89\right), \quad (6)$$

where t denotes time. The primary creep and secondary creep are determined by using the same method described for Type 1. The long duration of primary creep and the continuous secondary creep can also be observed in Figure 4b. Type 2 creep is evident in coal samples at pressures of 10.00 and 17.01 MPa.

In Type 3, after primary stage, the axial strain creeps at a nearly constant rate (Figure 4c), then, without obvious acceleration, the sample suddenly explodes into small fragments (Figure 7). This is consistent with the explosive failure of anthracite reported by Pomeroy [38]. The dominant radial strain shifts the volumetric strain from initial compressional behaviour to extensional strain in a very short time and then the strain increases at a very high rate until failure. From Figure 8, it is observed that the strain rates all gradually decelerate from their initial state to a stable stage and then end with a sudden rise. Compared to Type 1 and Type 2 creep curves, the data are less scattered, indicating a remarkable and continuous deterioration of the internal structure in the sample. Data fitting is not required, and no fitted curves are shown. By examining the radial strain (shown in Figure 8b), the primary creep, secondary creep, and tertiary creep are identified and presented in Figure 4c. The duration of tertiary creep is much shorter than it of the primary creep or the secondary creep, only accounts for 6.3% of the whole creep process. This indicates a rapid development of microcracks and subsequent explosive failure. Type 3 creep was observed in coal samples tested at 11.02, 15.99, and 17.97 MPa.

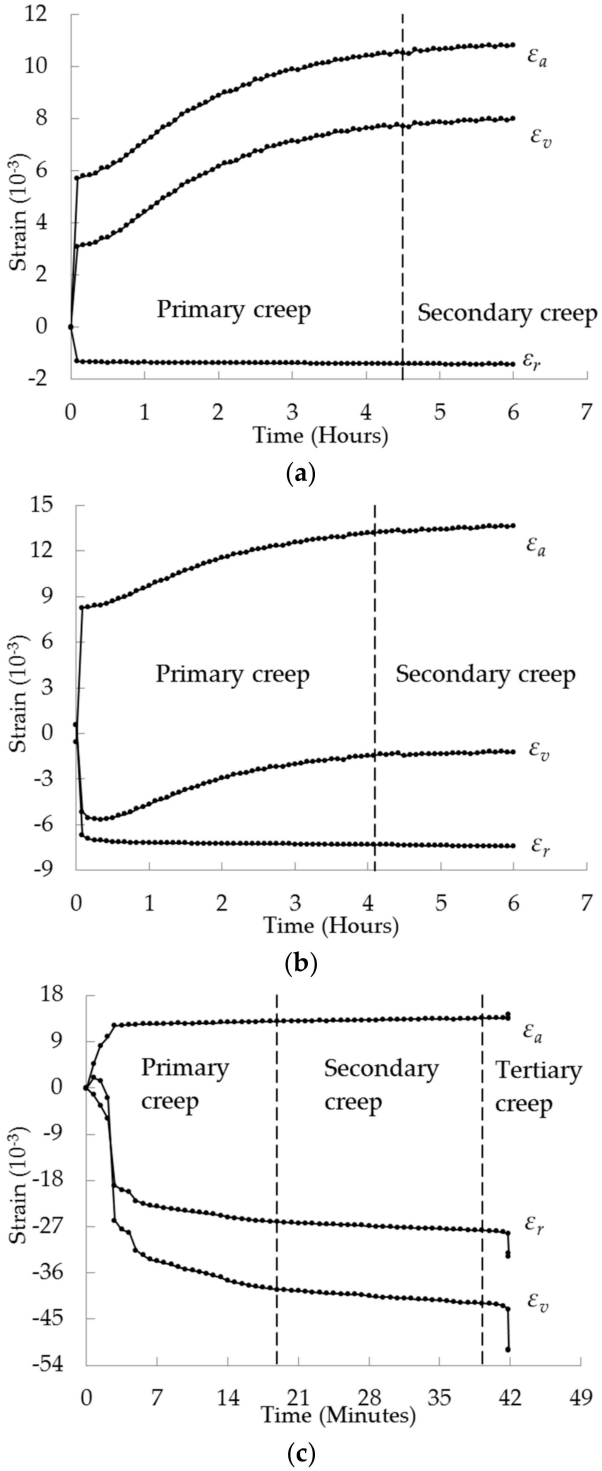

Figure 4. Creep curves for coal sample compressed at: (**a**) 8.03 MPa; (**b**) 17.01 MPa; (**c**) 11.02 MPa (dashlines denote the transition points of creep stages).

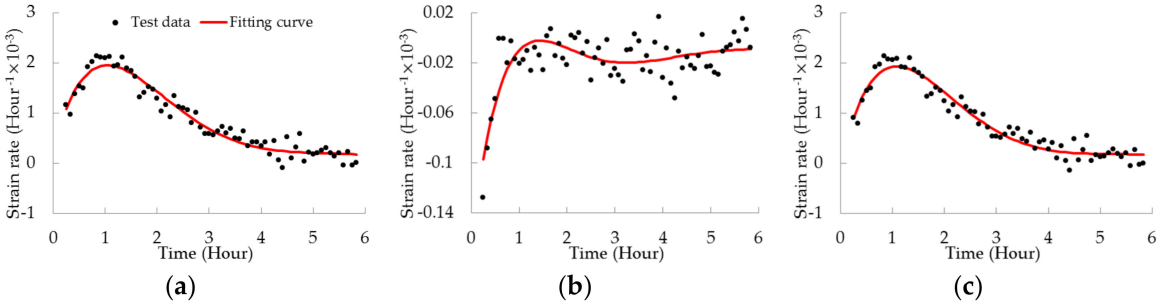

Figure 5. Strain rates versus time graphs for the coal sample compressed at 8.03 MPa: (**a**) axial strain rate (r_a); (**b**) radial strain rate (r_r); (**c**) volumetric strain rate (r_v).

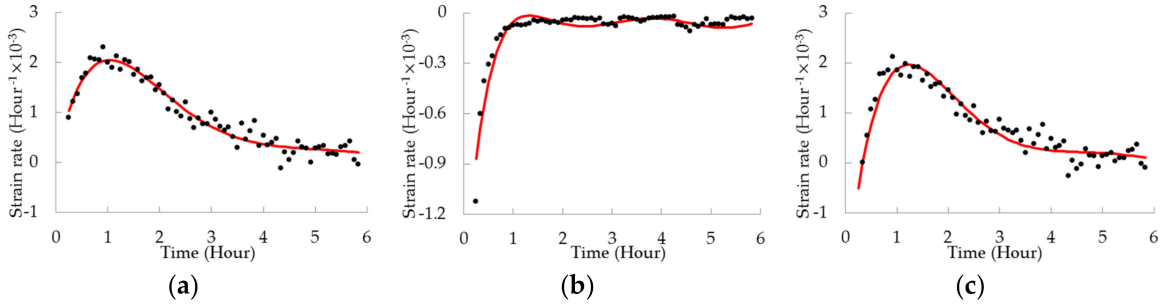

Figure 6. Strain rates versus time graphs for the coal sample compressed at 17.01 MPa: (**a**) axial strain rate (r_a); (**b**) radial strain rate (r_r); (**c**) volumetric strain rate (r_v).

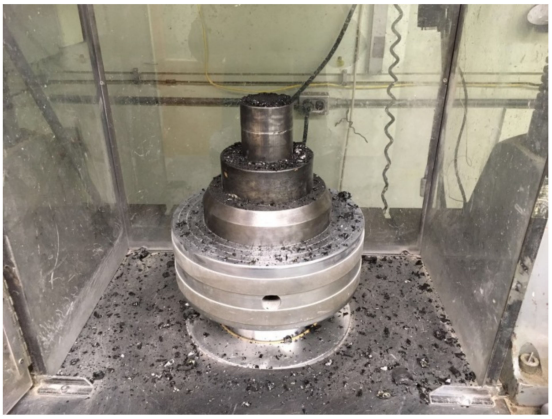

Figure 7. Photograph showing the remains of a typical anthracite sample after failure.

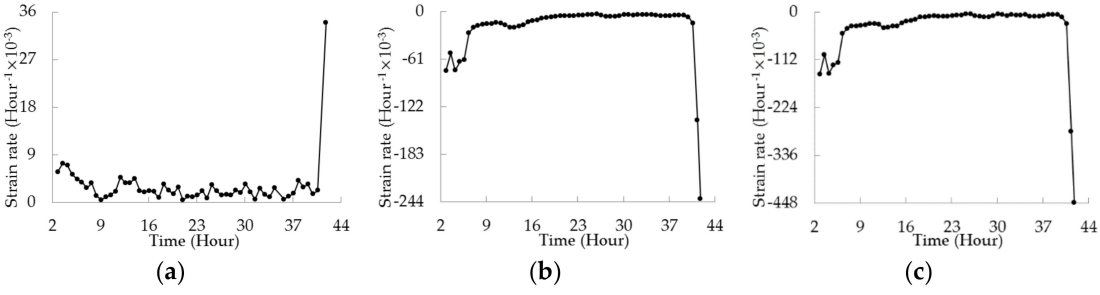

Figure 8. Strain rates versus time graphs for the coal sample compressed at 11.02 MPa: (**a**) axial strain rate (r_a); (**b**) radial strain rate (r_r); (**c**) volumetric strain rate (r_v).

3.2. Changes in Acoustic Wave Properties

In conventional creep characterisation studies, strain-time relationships are established on the assumption that the laboratory-scale sample is homogeneous so that the macroscopic deformation can be averaged over the whole sample to represent the mechanical responses of the rock material. However, the pronounced inhomogeneity of the coal samples used in this study introduced considerable irregularity into the creep strain data with increasing stress levels, which highlights the shortcomings of the conventional method for studying creep in coal. Therefore, in this section, ultrasonic wave velocities and attenuations measured during the creep tests are presented to provide more detailed information about the structural deformation within the samples.

The P- and S-wave velocities recorded during the creep tests were normalised by their initial values (v_{po} and v_{so}) and plotted versus time in Figure 9. Because the tests at 11.02, 15.99, and 17.97 MPa were of short duration, those data are plotted against a time scale in minutes (Figure 9b or Figure 9d). From Figure 9a or Figure 9c, it can be seen that the velocities of P- and S-waves from long-term creep during each creep test fluctuate moderately with similar amplitudes. During the creep tests, the fluctuations ranged from 7.2% to 2.1% for P-wave velocities and 6.9% to 1.8% for S-wave velocities. This implies that the internal structure was being continuously altered during the tests. However, the magnitudes of the velocities, and thus the forms of the fluctuation curves, vary significantly as the stress level is increased from ~8 MPa to ~17 MPa and the relationship cannot be formulated as any comprehensible mathematical equation. In contrast, the P- and S- wave velocities for the 11.02, 15.99, and 17.97 MPa tests all show a general downward trend (Figure 9b or Figure 9d). The overall declines are 5.4%, 4.9%, and 3.4% for P-wave velocities generated at of 11.02, 15.99, and 17.97 MPa, respectively, and the velocity decreases for S-waves at the same three pressures are 12.5%, 9.6%, and 7.7% (the data is supplemented in Table 2) The decrease of the S-wave velocities is about twice as large as that of the P-wave velocities. It is well known that the velocity of S-waves is more sensitive to microcracks oriented parallel to the propagating direction of wave (in this case, it is the loading direction), whereas P-wave velocity is more sensitive to the microcracks oriented perpendicular to the propagation direction of the ultrasound wave. Therefore, the larger decline in the S-wave velocities indicates that the main mechanism triggering sample failure is the development of microcracks parallel or subparallel to the sample's axis. Several previous studies using triaxial loading experiments on sandstone [42–44] observed that the S-wave/P-wave velocity decline ratio ranged from about 2.5 to 5, which is consistent with the results obtained by this work. The consistency of these results implies that, even when the materials being deformed are different and are subjected to different forms of stress, the damage generated in brittle rock materials may possibly be developed by the same mechanisms.

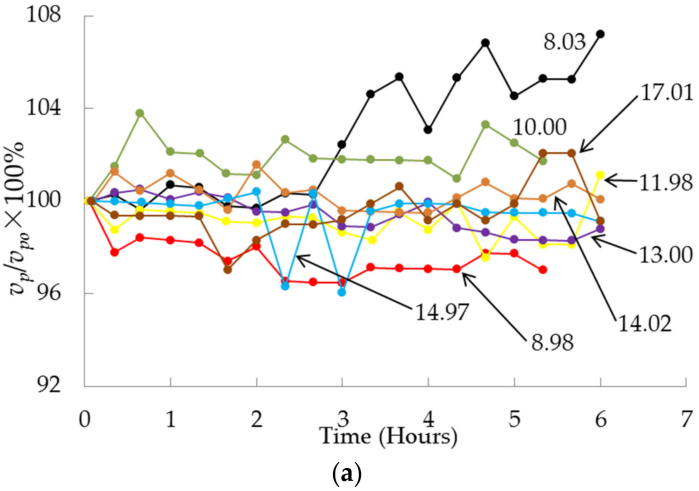

(**a**)

Figure 9. *Cont.*

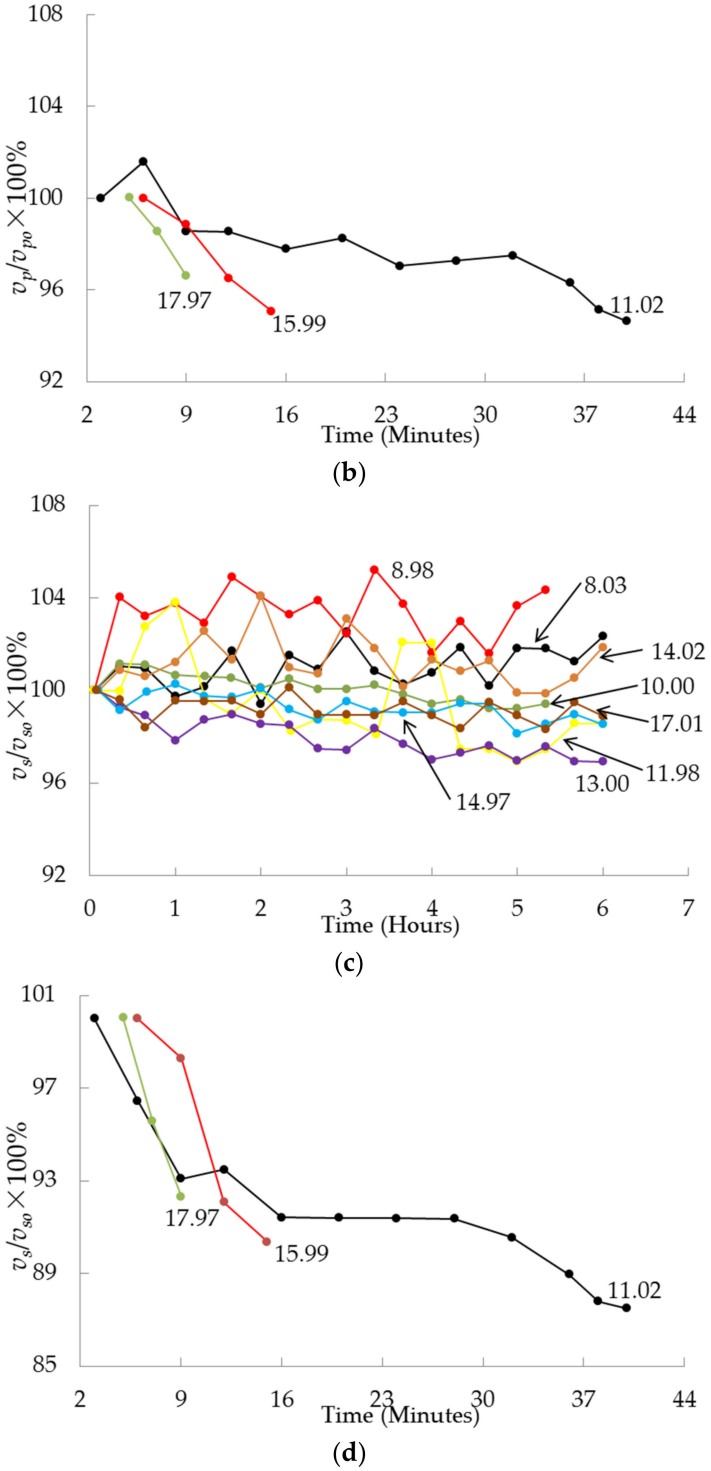

Figure 9. Graphs showing the changes in ultrasonic velocities during creep tests: (**a**) P-wave velocities of coal samples measured at 8.03 MPa, 8.98 MPa, 10.00 MPa, 11.98 MPa, 13.00 MPa, 14.02 MPa, 14.97 MPa, and 17.01 MPa; (**b**) P-wave velocities of coal samples measured at 11.02 MPa, 15.99 MPa, and 17.97 MPa; (**c**) S-wave velocities of coal samples measured at 8.03 MPa, 8.98 MPa, 10.00 MPa, 11.98 MPa, 13.00 MPa, 14.02 MPa, 14.97 MPa, and 17.01 MPa; (**d**) S-wave velocities of coal samples measured at 11.02 MPa, 15.99 MPa, and 17.97 MPa.

Table 2. Ultrasonic velocity data acquired during the short-term creep process.

Time (Minutes)	Change in P-Wave Velocity (100%)			Change in S-Wave Velocity (100%)		
	11.02 MPa	**15.99 MPa**	**17.97 MPa**	**11.02 MPa**	**15.99 MPa**	**17.97 MPa**
3	100.0	-	-	100.0	-	-
5	-	-	100.0	-	-	100.0
6	101.6	100.0	-	96.5	100	-
7	-	-	98.5	-	-	95.6
9	98.5	98.8	96.6	93.1	98.3	92.3
12	98.5	96.5		93.5	92.1	
15	-	95.1		-	90.4	
16	97.8			91.4		
20	98.3			91.4		
24	97.0			91.4		
28	97.3			91.4		
32	97.5			90.6		
36	96.3			89.0		
38	95.1			87.8		
40	94.6			87.5		

Given the complexities of the normalised ultrasonic wave velocity plotted in Figure 9a or Figure 9c, dynamic moduli (E_d) of the velocities were calculated to supplemented examination of the damage generated during creep. The moduli plotted in Figure 10 were calculated from Equation (7).

$$E_d = \frac{\rho v_s^2 \left(3v_p^2 - 4v_s^2\right)}{v_p^2 - v_s^2}, \quad (7)$$

where ρ is the bulk density of the sample. In order to reduce the effect of sample inhomogeneity on the calculated dynamic modulus, the modulus is normalised by the static modulus (E_s) for each sample, which are derived in uploading phase (listed in Table 3). As shown in Figure 10, despite accumulated damage from creep stress, the dynamic modulus is still 1.2–3.7 times higher than the static modulus. This discrepancy is larger than that reported by other researchers [45–47] and can be attributed to the presence of numerous fractures, cracks, and voids in the coal samples; an example is shown in Figure 11. These defects contribute significantly to the plastic deformation involved in uploading phase, resulting in a low static modulus. As is clear from Figure 10, there is not a unified correlation between normalised dynamic modulus and stress level. The moduli of unbroken samples (Figure 10a) are consistently larger than those of failed samples (Figure 10b), and this reflects different responses to long-term and short-term creep. Specifically, the normalised dynamic modulus for short-term creep is negatively related to the stress level, but long-term creep and stress level show no obvious correlation.

Table 3. Static moduli attained from uploading phase.

Creep Stress (MPa)	Static Modulus (GPa)
8.03	1.31
8.98	1.29
10.00	1.89
11.02	1.63
11.98	1.82
13.00	1.89
14.02	1.58
14.97	2.25
15.99	2.04
17.01	2.43
17.97	3.49

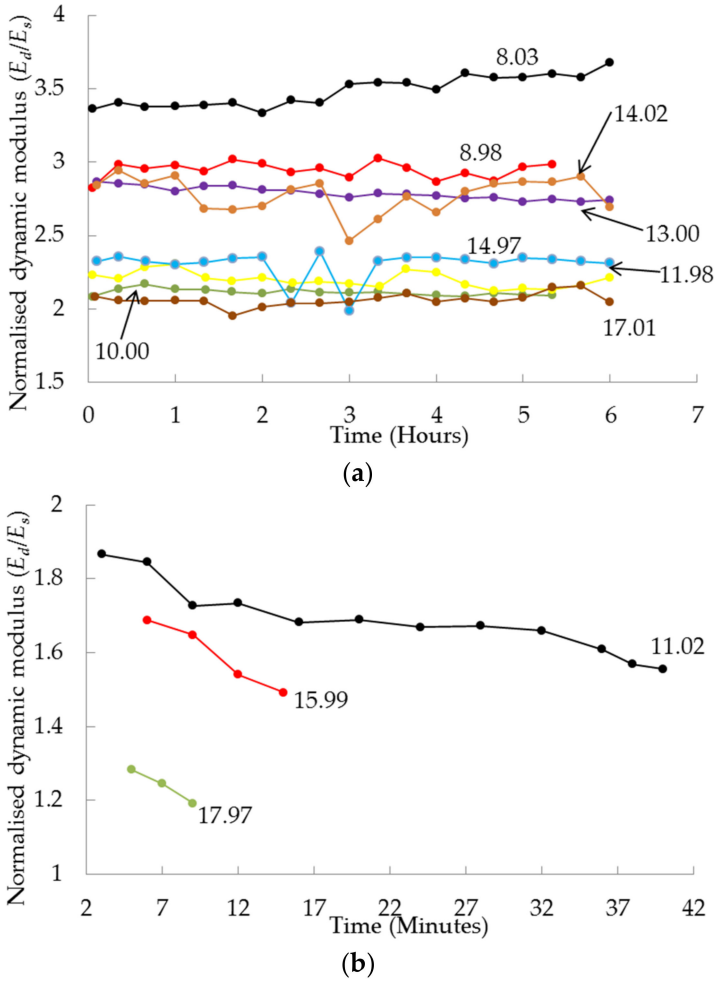

Figure 10. Normalised dynamic moduli versus time during creep tests for: (**a**) unbroken samples; (**b**) broken samples. The numbers denote the samples tested at 8.03 MPa, 8.98 MPa, 10.00 MPa, 11.02 MPa, 11.98 MPa, 13.00 MPa, 14.02 MPa, 14.97 MPa, 15.99 MPa, 17.01 MPa, and 17.97 MPa, respectively.

Figure 11. Photograph of a coal sample showing numerous voids and cracks.

Concerning short-term creep, the previous discussion about P-wave velocities declining less than S-wave velocities showed that the underlying mechanism triggering violent failure of the coal samples is the development of vertical cracks. The negative correlation of broken samples and stress level indicates that the magnitude of this structural deterioration is controlled by the stress level. In addition, it is interesting to note in Figure 10b that, although the normalised dynamic modulus consistently decreases with time, the modulus ratio does not decline significantly at failure, as is commonly the case at the end of compression tests [48–50]. The average percentage decrease for the normalised dynamic modulus in this study is only 12%, thus considerable stiffness must still remain when the sample is near failure. In order to illustrate this phenomenon, a sketch showing the structural deformation inside a sample of coal is included as Figure 12. During uploading phase, vertical cracks develop and transform the sample into a structure consisting of several separated columns. This process does not significantly weaken the bearing capacity of the sample to the vertical pressure, but deteriorates its resistance to the lateral perturation. When creep begins, the structure of the sample becomes very sensitive to the localized shear and tensile failures. When creep compression continues, the vertical cracks gradually enlarge but have only a slight influence on the axial strain and the stiffness. However, this deterioration increases the possibility of tensile and shear failures of individual columns and this would trigger the sudden release of strain energy. Eventually, the violent collapse turns the already fragile structure into fragments.

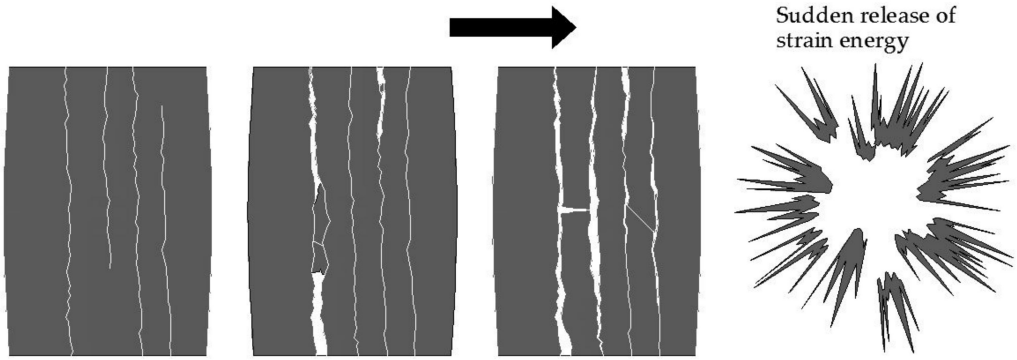

Figure 12. Sketch showing the creep stress induced deterioration in a sample of anthracite. The arrow indicates the progression of structural degradation.

As for long-term creep, in spite of the measures to reduce the effects of sample inhomogeneity, the variations in the normalised dynamic moduli are still independent of stress level to a certain extent. This suggests that the structural deformation in the sample is not completely dominated by the compression-induced tensile cracking just described above. Further evidence can be obtained by examining the fluctuations of the normalised dynamic moduli over time. Except for the relatively stable moduli at 10.00 MPa and 13.00 MPa, all of the moduli in Figure 10a exhibit fluctuations that are difficult to explain with a single deformational mechanism. We attributed the fluctuations to the active involvement of multiple structural deformations such as particle dislocation, pore closure, matrix cracking, compaction of clay mineral, and so forth. It has been shown that ultrasonic velocity is determined by the fastest wave front passing through the most favourable portion of the rock. In practice, this means the velocity is the speed of the wave front affected by the fewest defects [51]. However, the multiple deformations alter the internal structure of the sample in different ways over long periods of time and this results in the ultrasonic velocity (and its dynamic modulus) fluctuating. This means a more precise ultrasonic parameter is required to interpret the inner deformational mechanisms of long-term creep correctly. Martínez-Martínez et al. [51] proposed a spatial attenuation parameter (α_s) summing the wave attenuation caused by both defects and discontinuities in the rock. Hence, this parameter should allow an investigator to improve their assessment of the deformation

in the sample. This spatial attenuation parameter is thus is a more appropriate tool for evaluating long-term creep data. The α_s is expressed as

$$\alpha_s = \frac{20 \times log\left(\frac{A_{m1}}{A_{m2}}\right)}{L}, \quad (8)$$

where A_{m1} is the maximum amplitude generated by the transducer, A_{m2} is the maximum amplitude recorded by the receiver, and L is the length of the sample.

By using Equation (8), the spatial attenuation parameters for long-term creep can be obtained. As explained in Section 3.1, for this investigation creep has been classified into three types. In order to explore the deformation underlying different creep mechanisms, the spatial attenuation parameters and the fitting curves for Types 1 and 2 strain rates are plotted versus time in Figures 13 and 14, respectively. (In Figure 13, two sets of representative experimental data are selected to present). In contrast to the irregular fluctuations observed in ultrasonic velocities and dynamic moduli, the spatial attenuation parameters show clear trends. For Type 1 creep, the spatial attenuation parameters at both ~8 MPa and ~12 MPa gradually decline to a relatively stable value and then begin to rise. The initial reduction is expected because the samples are being subjected to a high compressive strain rate along their axis which results in a denser packing pattern along the direction of axial stress, but the subsequent flat and increasing portions of the curve cannot be explained by compression. Through examining the correlation between the strain rates and the spatial attenuation parameter, we found that the presence of the transition point (from the decline to a stable stage) of α_s is slightly later than it of the peak value of axial strain rate. The peak of axial strain rate is the beginning of the deceleration of compaction. Obviously, a different mechanism balances the influence of compaction on attenuation and tends to dominate the αs curve at the stage of secondary creep. The most probable mechanism that can achieve this result is micro-cracking in the coal matrix. The competition between compaction and micro-cracking can also be seen on the spatial attenuation curves for Type 2 creep (Figure 14). Both the ~10 MPa and the ~17 MPa curves show a small increase at initial dilatancy (corresponding to a high radial strain rate) and then follow a downtrend similar to the Type 1 curves when axial compression begins to dominate the creep. The shift point to a moderate increase still closely follows the beginning of the deceleration of compaction, indicating that micro-cracking temporarily becomes a more important mechanism than compaction. However, this increase lasts only 1.5 h and 1 h for samples compressed at 10.00 MPa and 17.01 MPa, respectively, before becoming a stable phase. The stable phase then lasts until the end of test and must mean that the influences of micro-cracking and compression are balanced.

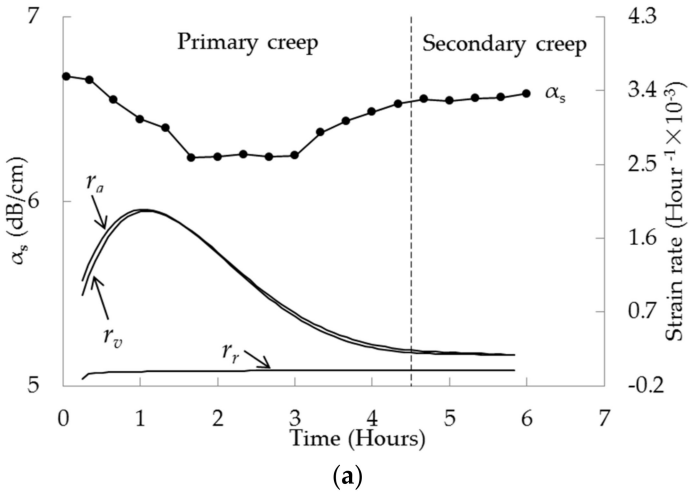

(**a**)

Figure 13. *Cont.*

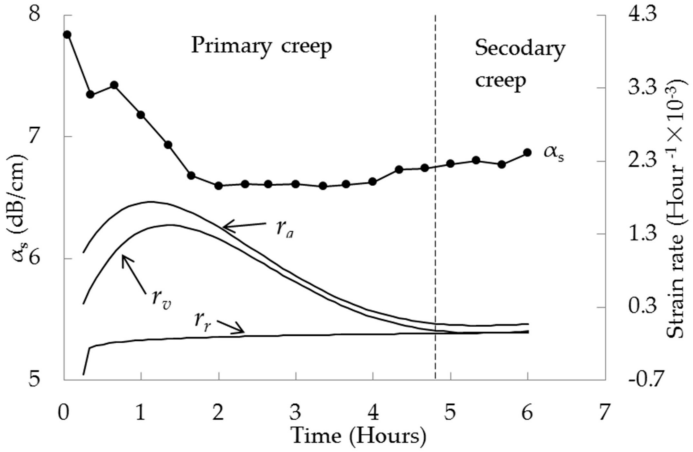

Figure 13. Graphs showing the spatial attenuation parameters and strain rates plotted versus time for Type 1 creep. Results are shown for tests at; (**a**) 8.03 MPa; (**b**) 11.98 MPa. r_a, r_v, r_r, and α_s denote axial strain rate, volumetric strain rate, radial strain rate, and spatial attenuation parameter, respectively. The dashlines denote the transition points of creep stages.

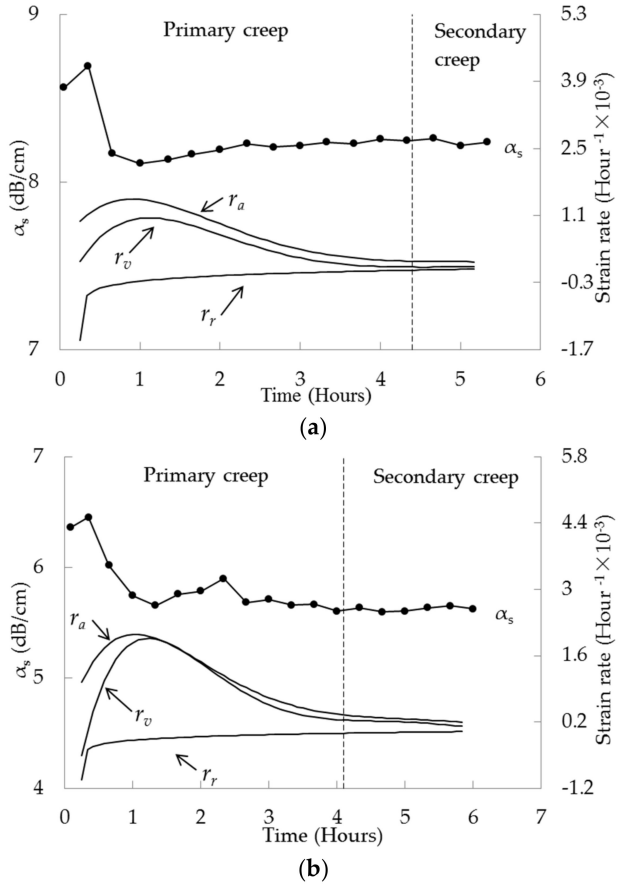

Figure 14. Graphs showing the spatial attenuation parameters and strain rates plotted versus time for Type 2 creep. Results are shown for tests at: (**a**) 10.00 MPa; (**b**) 17.01 MPa. r_a, r_v, r_r, and α_s denote axial strain rate, volumetric strain rate, radial strain rate, and spatial attenuation parameter, respectively. The dashlines denote the transition points of creep stages.

Motivated by curiosity, we also calculated the spatial attenuation parameter for short-term creep corresponding to Type 3 creep. Two sets of representative data are shown in Figure 15, data for the tests at 11.02 MPa and 15.99 MPa. Probably reflecting the development of vertical cracks depicted in Figure 12, both spatial attenuation curves end with an apparent increase. An initial decline and a U-shaped curve are evident for the sample compressed at 11.02 MPa; this clearly reflects the competition between compaction and cracking. As for the sample compressed at 15.99 MPa, if the interval of sampling were small enough, a curve of similar shape might be visible. During the stages of secondary creep and tertiary creep, the increase of both spatial attenuation curves indicate a dramatic development of micro-cracks, which can also be verified by the high volumetric strain rate and radial strain rate. These observations appear to confirm an inherent consistency between short-term and long-term creep. The mechanical response of samples under creep compression is a result of competition between compaction and cracking, in which the cracking deteriorates the structure and increases the ultrasonic attenuation, whilst the compaction causes the densification along axial axis and reduces attenuation.

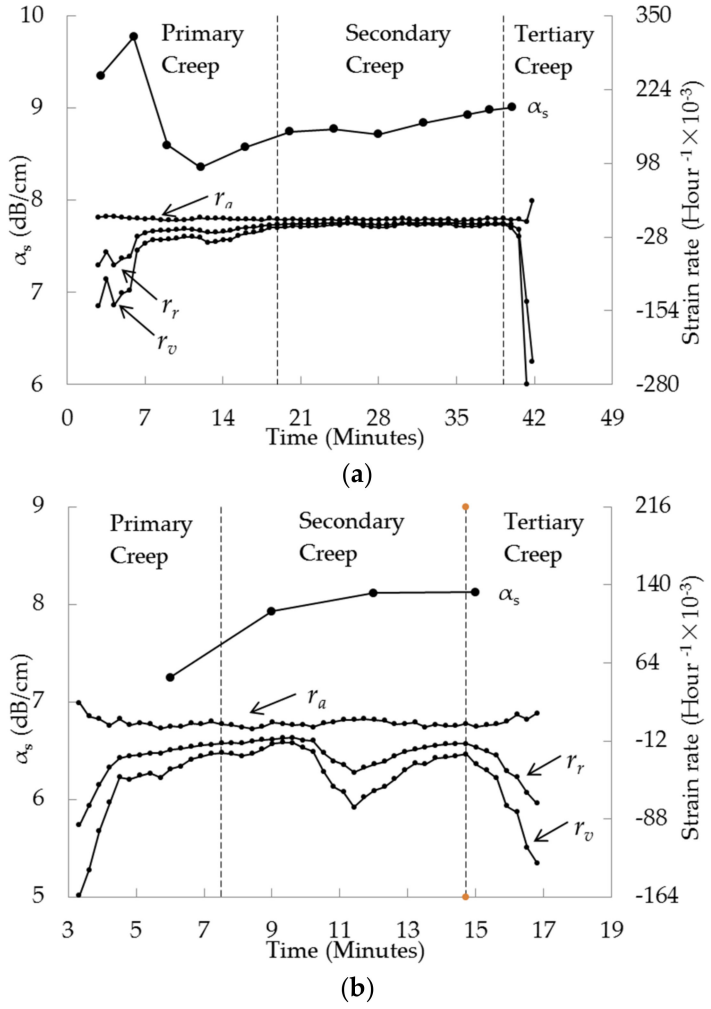

Figure 15. Graph of spatial attenuation parameters and strain rates versus time for Type 3 creep. Results are shown for tests at: (**a**) 11.02 MPa; (**b**) 15.99 MPa. r_a, r_v, r_r, and α_s denote axial strain rate, volumetric strain rate, radial strain rate, and spatial attenuation parameter, respectively. The dashlines denote the transition points of creep stages.

4. Implications and Future Work

The coal pillar bump and abrupt collapse of roadway rib has been a major problem faced by coal mining practitioners for several decades. These violent failures are a result of the long-term accumulation of mechanical damage caused by overburden pressure. However, due to the invisibility of mechanical damage, there is a lack of an effective method to quantify the damage accumulation and predict the subsequent failure. So far, the most common method for failure forecasting is still based on the long-term measurement of coal surface deformation. This method is costly, time-consuming, and imprecise. Moreover, there is not a convincing theory relating the surface deformation to the mechanical damage, because the damage is the cumulative destruction of bonds in the rock's microstructure [52]. Therefore, it cannot be directly measured by macroscopic scale tests. In view of this situation, we devote this study to explore the applicability of the ultrasonic technique in the investigation of the inner structural deformation of coal under creep compression. The implications of this study for practitioners can be summarised as follows: (1) The long-term coal creep is a multiple structural deformation involving of particle dislocation, pore closure, matrix cracking, compaction of clay mineral, and so forth. It continuously alters the coal structure, resulting in the fluctuations of ultrasonic velocity and associated dynamic modulus. Therefore, the capacity of ultrasonic velocity parameter for damage detection is greatly weakened. (2) The acoustic attenuation parameter can make a comprehensive evaluation of the structural deformation, reflecting the competition between compaction and cracking during the creep process. (3) The coal is characterised by a strong inhomogeneity, showing a high sample-to-sample scatter in mechanical properties. Conventional test methods that are successful in the characterisation of other rock types cannot be used for coal. Therefore, the non-destructive testing technique which can achieve a repetitive measurement in a single sample is much suitable.

The unsolved problems of this study are (1) the relationship between the inhomogeneity of coal and the explosive failure mode is still remained unknown and (2) the influences of compaction and micro-cracking on acoustic attenuation have not been quantified. These problems will be investigated in the future work by enlarging the sample size and introducing the CT scanning technique.

5. Conclusions

The inner structural variation of an extremely inhomogeneous coal subjected to incremental creep stress has been experimentally investigated by monitoring both the macroscopic deformation and the acoustic wave properties. Based on ultrasonic velocities, attenuations, and dynamic moduli, the deformational mechanisms underlying macroscopic deformations are discussed. The main conclusions are as follows:

(1) The pronounced inhomogeneity of coal induces considerable irregularities in creep strain data collected during the increase of stress level. These flawed data highlight the shortcomings of conventional strain–time relationship experiments for deciphering the mechanisms that control creep.
(2) The mechanical response of samples under creep compression is a result of competition between compaction and cracking, in which the cracking deteriorates the structure and increases the ultrasonic attenuation, whilst the compaction causes the densification along axial axis and reduces attenuation.
(3) Long-term creep involves multiple structural deformations that alter the internal structure of sample, thus resulting in fluctuation of the ultrasonic velocities and the dynamic moduli.
(4) During uploading phase of short term creep, vertical cracks develop and transform the sample into a structure consisting of separated columns. Further deterioration of the coal increases the possibility of tensile and shear failure of individual columns, which can trigger the violent collapse of an already fragile structure.

Acknowledgments: This work was financially supported by the Fundamental Research Funds for the Central Universities (2017CXNL01).

Author Contributions: Sen Yang proposed the idea; Sen Yang and Nong Zhang designed and performed the experiments; Sen Yang and Xiaowei Feng analyzed the data; Jiaguang Kan and Nong Zhang provided suggestions and assisted Sen Yang in revising the manuscript. Sen Yang wrote and revised the manuscript. All authors agree to be listed and approve the submitted and accepted versions of the publication.

Conflicts of Interest: The authors declare no conflict of interest.

References

1. International Energy Agency. *World Energy Outlook 2017*; Organisation for Economic Co-Operation and Development (OECD): Paris, France, 2017.
2. Liang, M.; Fang, X. Application of Fiber Bragg Grating Sensing Technology for Bolt Force Status Monitoring in Roadways. *Appl. Sci.* **2018**, *8*, 107. [CrossRef]
3. He, M.C.; Xie, H.P.; Peng, S.P.; Jiang, Y.D. Study on rock mechanics in deep mining engineering. *Chin. J. Rock Mech. Eng.* **2005**, *24*, 2803–2813. (In Chinese)
4. Li, T.; Cai, M.F.; Cai, M. A Review of Mining-Induced Seismicity in China. *Int. J. Rock Mech. Min. Sci.* **2007**, *44*, 1149–1171. [CrossRef]
5. Ma, Z.; Gu, R.; Huang, Z.; Peng, G.; Zhang, L.; Ma, D. Experimental Study on Creep Behavior of Saturated Disaggregated Sandstone. *Int. J. Rock Mech. Min. Sci.* **2014**, *66*, 76–83. [CrossRef]
6. Hatt, W.K. *Notes on the Effect of Time Element in Loading Reinforced Concrete Beams*; ASTM: Philadelphia, PA, USA, 1907.
7. Washa, G.W.; Fluck, P.G. Plastic Flow (Creep) of Reinforced Concrete Continuous Beams. *ACI Struct. J.* **1956**, *52*, 549–561.
8. Dragon, A.; Mroz, Z. A Continuum Model for Plastic Brittle Behavior of Rock and Concrete. *Int. J. Eng. Sci.* **1979**, *17*, 121–137. [CrossRef]
9. Altoubat, S.A.; Lange, D.A. Creep, Shrinkage, and Cracking of Restrained Concrete at Early Age. *ACI Mater. J.* **2001**, *98*, 323–331.
10. Yuan, Y.; Wan, Z.L. Prediction of Cracking within Early-Age Concrete due to Thermal, Drying and Creep Behavior. *Cem. Concr. Res.* **2002**, *32*, 1053–1059. [CrossRef]
11. Benboudjema, F.; Meftah, F.; Torrenti, J.M. Interaction between Drying, Shrinkage, Creep and Cracking Phenomena in Concrete. *Eng. Struct.* **2005**, *27*, 239–250. [CrossRef]
12. Bažant, Z.P.; Hauggaard, A.B. Microprestress-Solidification Theory for Concrete Creep I: Aging and Drying Effects. *J. Eng. Mech.* **1997**, *123*, 1188–1194. [CrossRef]
13. Bažant, Z.P.; Prasannan, S. Solidification Theory for Concrete Creep. I: Formulation and II. Verification and Application. *J. Eng. Mech.* **1997**, *123*, 1691–1725. [CrossRef]
14. Bažant, Z.P. Prediction of Concrete Creep Effects Using Age-Adjusted Effective Modulus Method. *J. Am. Concr. Inst.* **1972**, *69*, 212–217.
15. Bažant, Z.P.; Najjar, L.J. Comparison of Approximate Linear Methods for Concrete Creep. *J. Struct. Div.* **1973**, *99*, 1851–1874.
16. Glanville, W.H. *Studies in Reinforced Concrete: The Creep or Flow of Concrete under Load*; HM Stationery Office: Richmond, UK, 1930.
17. Shrestha, K.M.; Chen, B.C.; Chen, Y.F. State of the Art of Creep of Concrete Filled Steel Tubular Arches. *KSCE J. Civ. Eng.* **2011**, *15*, 145–151. [CrossRef]
18. Maslov, G.N. Thermal Stress States in Concrete Masses, with Account of Concrete Creep. *Izvestia Nauchno-Issledovatel'skogo Instituta Gidrotechniki* **1940**, *28*, 175–188.
19. Bažant, Z.P.; Baweja, S. Creep and Shrinkage Prediction Model for Analysis and Design of Concrete Structures: Model B3. *ACI Spec. Publ.* **2000**, *194*, 1–84.
20. Bažant, Z.P.; Osman, E. Double Power Law for Basic Creep of Concrete. *Matériaux Constr.* **1976**, *9*, 3–11. [CrossRef]
21. Griggs, D. Creep of Rocks. *J. Geol.* **1939**, *47*, 225–251. [CrossRef]
22. Carter, N.L.; Hansen, F.D. Creep of Rocksalt. *Tectonophysics* **1983**, *92*, 275–333. [CrossRef]

23. Cruden, D.M.; Masoumzadeh, S. Accelerating Creep of the Slopes of a Coal Mine. *Rock Mech. Rock Eng.* **1987**, *20*, 123–135. [CrossRef]
24. Scott Duncan, E.J.; Lajtai, E.Z. The Creep of Potash Salt Rocks from Saskatchewan. *Geotech. Geol. Eng.* **1993**, *11*, 159–184. [CrossRef]
25. Drescher, K.; Handley, M.F. Aspects of Time-Dependent Deformation in Hard Rock at Great Depth. *J. S. Afr. Inst. Min. Metall.* **2003**, *103*, 325–336.
26. Fabre, G.; Pellet, F. Creep and Time-Dependent Damage in Argillaceous Rocks. *Int. J. Rock Mech. Min. Sci.* **2006**, *43*, 950–960. [CrossRef]
27. Heap, M.J.; Baud, P.; Meredith, P.G.; Bell, A.F.; Main, I.G. Time-Dependent Brittle Creep in Darley Dale Sandstone. *J. Geophys. Res. Solid Earth* **2009**, *114*, 1–22. [CrossRef]
28. Zhou, H.W.; Wang, C.P.; Han, B.B.; Duan, Z.Q. A Creep Constitutive Model for Salt Rock Based on Fractional Derivatives. *Int. J. Rock Mech. Min. Sci.* **2011**, *48*, 116–121. [CrossRef]
29. Yang, D.; Bornert, M.; Chanchole, S.; Wang, L.; Valli, P.; Gatmiri, B. Experimental Investigation of the Delayed Behavior of Unsaturated Argillaceous Rocks by Means of Digital Image Correlation Techniques. *Appl. Clay Sci.* **2011**, *54*, 53–62. [CrossRef]
30. Yang, D.S.; Chen, L.F.; Yang, S.Q.; Chen, W.Z.; Wu, G.J. Experimental Investigation of the Creep and Damage Behavior of Linyi Red Sandstone. *Int. J. Rock Mech. Min. Sci.* **2014**, *72*, 164–172. [CrossRef]
31. Mishra, B.; Verma, P. Uniaxial and Triaxial Single and Multistage Creep Tests on Coal-Measure Shale Rocks. *Int. J. Coal Geol.* **2015**, *137*, 55–65. [CrossRef]
32. Bikong, C.; Hoxha, D.; Shao, J.F. A Micro-Macro Model for Time-Dependent Behavior of Clayey Rocks due to Anisotropic Propagation of Microcracks. *Int. J. Plast.* **2015**, *69*, 73–88. [CrossRef]
33. Zhang, Y.; Shao, J.; Xu, W.; Jia, Y. Time-Dependent Behavior of Cataclastic Rocks in a Multi-Loading Triaxial Creep Test. *Rock Mech. Rock Eng.* **2016**, *49*, 3793–3803. [CrossRef]
34. Boukharov, G.N.; Chanda, M.W.; Boukharov, N.G. The Three Processes of Brittle Crystalline Rock Creep. *Int. J. Rock Mech. Min. Sci. Geomech. Abstr.* **1995**, *32*, 325–335. [CrossRef]
35. Jaeger, J.C.; Cook, N. *Fundamentals of Rock Mechanics*; Blackwell Pub.: Malden, MA, USA, 2007.
36. Kang, J.; Zhou, F.; Liu, C.; Liu, Y. A Fractional Non-Linear Creep Model for Coal Considering Damage Effect and Experimental Validation. *Int. J. Non-Linear Mech.* **2015**, *76*, 20–28. [CrossRef]
37. Scholz, C.H. Mechanism of Creep in Brittle Rock. *J. Geophys. Res.* **1968**, *73*, 3295–3302. [CrossRef]
38. Pomeroy, C.D. Creep in Coal at Room Temperature. *Nature* **1956**, *178*, 279. [CrossRef]
39. Kaiser, P.K.; Morgenstern, N.R. Time-Dependent Deformation of Small Tunnels-II. Typical Test Data. *Int. J. Rock Mech. Min. Sci.* **1981**, *18*, 141–152. [CrossRef]
40. Yang, S.Q.; Xu, P.; Ranjith, P.G. Damage Model of Coal under Creep and Triaxial Compression. *Int. J. Rock Mech. Min. Sci.* **2015**, *80*, 337–345. [CrossRef]
41. Bieniawski, Z.T.; Bernede, M.J. Suggested Methods for Determining the Uniaxial Compressive Strength and Deformability of Rock Materials: Part 1. Suggested Method for Determination of the Uniaxial Compressive Strength of Rock Materials. *Int. J. Rock Mech. Min. Sci.* **1979**, *16*, 135–140. [CrossRef]
42. Sammonds, P.R.; Ayling, M.R.; Meredith, P.G.; Murrell, S.A.F.; Jones, C. A laboratory investigation of acoustic emission and elastic wave velocity changes during rock failure under triaxial stresses. In Proceedings of the ISRM International Symposium, Pau, France, 30 August–2 September 1989.
43. Ayling, M.R.; Meredith, P.G.; Murrell, S.A.F. Microcracking during Triaxial Deformation of Porous Rocks Monitored by Changes in Rock Physical Properties, I. Elastic-Wave Propagation Measurements on Dry Rocks. *Tectonophysics* **1995**, *245*, 205–221. [CrossRef]
44. Fortin, J.; Guéguen, Y.; Schubnel, A. Effects of Pore Collapse and Grain Crushing on Ultrasonic Velocities and Vp/Vs. *J. Geophys. Res. Solid Earth* **2007**, *112*, 1–16. [CrossRef]
45. Guéguen, Y.; Palciauskas, V. *Introduction to the Physics of Rocks*; Princeton University Press: Princeton, NJ, USA, 1994; pp. 159–167.
46. Al-Shayea, N.A. Effects of Testing Methods and Conditions on the Elastic Properties of Limestone Rock. *Eng. Geol.* **2004**, *74*, 139–156. [CrossRef]
47. Martínez-Martínez, J.; Benavente, D.; García-del-Cura, M.A. Comparison of the Static and Dynamic Elastic Modulus in Carbonate Rocks. *Bull. Eng. Geol. Environ.* **2012**, *71*, 263–268. [CrossRef]

48. Hallbauer, D.K.; Wagner, H.; Cook, N.G.W. Some Observations Concerning the Microscopic and Mechanical Behaviour of Quartzite Specimens in Stiff, Triaxial Compression Tests. *Int. J. Rock Mech. Min. Sci. Geomech. Abstr.* **1973**, *10*, 713–726. [CrossRef]
49. Kim, Y.-S.; Tatsuoka, F.; Ochi, K. Deformation Characteristics at Small Strains of Sedimentary Soft Rocks by Triaxial Compression Tests. *Geotechnique* **1994**, *44*, 461–478. [CrossRef]
50. Peng, R.; Ju, Y.; Wang, J.G.; Xie, H.; Gao, F.; Mao, L. Energy Dissipation and Release During Coal Failure Under Conventional Triaxial Compression. *Rock Mech. Rock Eng.* **2014**, *48*, 509–526. [CrossRef]
51. Martínez-Martínez, J.; Benavente, D.; García-del-Cura, M.A. Spatial Attenuation: The Most Sensitive Ultrasonic Parameter for Detecting Petrographic Features and Decay Processes in Carbonate Rocks. *Eng. Geol.* **2011**, *119*, 84–95. [CrossRef]
52. Gatelier, N.; Pellet, F.; Loret, B. Mechanical Damage of an Anisotropic Porous Rock in Cyclic Triaxial Tests. *Int. J. Rock Mech. Min. Sci.* **2002**, *39*, 335–354. [CrossRef]